
Article:
Davis, N.B., Waibel, K., Wang, K. et al. (2017) Microstructure of single-droplet granules formed from ultra-fine powders. Powder Technology, 305. pp. 19-26. ISSN: 0032-5910

https://doi.org/10.1016/j.powtec.2016.09.033

Microstructure of single-droplet granules formed from ultra-fine powders

Nathan B. Davis[1], Karis Waibel[1], Kelly Wang[1], James D. Litster[1,2]

1) Department of Chemical Engineering, Purdue University
2) School of Industrial and Physical Pharmacy, Purdue University
jlitster@purdue.edu

1. Abstract

A quantitative analysis of variations in granule microstructure based upon changes in primary particle size and bed preparation is presented. The granule microstructures are obtained using X-Ray Computed Tomography (XRCT). An algorithm is developed to measure the number and size of macro-voids (pore space with volume equivalent size greater than or equal to 30 μm or 3 times the primary particle size). Four size fractions of alumina, ranging in primary particle size from 0.5 μm to 108 μm, are sieved using three different sieve sizes to create static powder beds from which single-droplet granules are produced. The analysis shows that large macro-voids exist in ultra-fine powders (0.1-10 μm). The macro-voids take up to 7% of the granule volume and the largest macro-voids are 200-700 μm in volume equivalent size. Changing the sieve preparation changes the size and total volume of macro-voids. In contrast, there are very few macro-voids in granules formed from coarser powders. This study shows that micron sized powders have the opportunity to form complex structures during granulation and that the handling history of the materials should receive greater scrutiny than it currently gets.

2. Introduction

Wet granulation is a process by which small particles are formed into larger agglomerates through the use of a liquid binder. It has found application in a variety of industries, from pharmaceuticals, agriculture and food to ore processing and pigments[1]. A common application is to take fine particles and bind them to form high density agglomerates. These agglomerates may be the final product or they may be further compacted to make ribbons or tablets.

Most fundamental studies of wet granulation have used model materials, such as glass ballotini, or lactose. These materials often have a relatively large mean size (>20 μm). The study of ultra-fine particles (0.1-10 μm) behavior in wet granulation is uncommon, despite the fact that many powders of industrial interest for detergents, pigments, agricultural chemicals and ceramics are in this size range. As the primary particle size is reduced below 10 μm**,** van der Waals forces increase to a point at which they become non-negligible and capable of countering the weight of the individual particles [2]. The exact magnitude of this force also depends on particle shape and roughness, surface properties and the particle size distribution. Van der Waals forces can lead to self-agglomeration of the dry primary particles, resulting in complex and potentially unwanted behaviors and making the powder behavior very sensitive to its prior history. In their study of

drop penetration time, Hapgood et. al [3] found that their model was effective in all cases except when used for ultrafine powders (zinc oxide and titanium dioxide). Their penetration model assumes an effective porosity which is not as accurate for ultrafine powder beds which are expected to have a more complex microstructure than model materials. The study of hydrophobic nucleation mechanisms by Eshtiaghi et. al. [4–6] showed the formation of hollow and collapsed granules while using X-ray computed tomography (XRCT) to confirm their structural observations. However, their work used a variety of materials, ranging in size from 0.01-320 μm and these structures are not unique to the ultrafine powders. There are a few other studies in the wet granulation literature which make use of ultrafine powders [7–19]. Often, only one of several materials used was in the ultrafine range [3–9].

Hapgood et al. [3] and Emady et al. [7] studied the granule nucleation mechanism and their external structures. Emady et al. [7]identified that static bed granules will nucleate either through the Tunneling or the Spreading/Crater mechanism dependent upon the granule Bond number. Ultra-fine powders had low bond numbers and generally exhibited Tunneling behavior. Rough et al. [11,14,16] studied a semi-solid paste in a high-shear mixer for detergent granulation using an ultra-fine sodium alumino-silicate powder. Their work looked at the agglomeration mechanisms, bulk density characterization, and effects of solid formulations. Afarani et al. [13] showed, for alumina in a high-shear environment, that increasing binder content led to a wide size distribution, enhanced attrition and bulk compression strength of sintered granules, but provide only some SEM images for structural examination. There is additional work on hydrophobic granulation from Hapgood and Khanmohammadi [9] as well as Charles-Williams et al. [10] showing layering of hydrophobic particles on the outside of granules that are either hollow or filled with hydrophilic particles. None of these papers examine the potentially interesting behaviors that are unique to ultrafine powders. It is necessary to look outside of traditional wet granulation processes to find information about the interesting and complex behavior of ultrafine powders.

There are examples of other processes using ultrafine powders to create granules and agglomerates with a variety of internal structures. The internal structure of these agglomerates has an impact on its behavior during further processing. For example, Eckhard and Nebelung [20] showed a change from ductile to brittle behavior in the compaction of spray dried agglomerates by changing the structure from homogeneous to inhomogeneous. Inhomogeneous or “hollow” spray-dried granules can be created by using a well dispersed suspension which allows for particle mobility during drying. A different technique used by Pagnoux et al. [21] makes large, spherical granules in suspension through continuous stirring of primary agglomerates created from alumina (0.4 μm average) and silica (25 nm). The granule structure was changed from solid to hollow by adding a step to the primary agglomeration stage, producing a narrower primary agglomerate distribution. Fluidized beds have also been used to create soft agglomerates (non-

permanent bonds) in cohesive nano- and micro-powders where the van der Waals forces are dominant [22–29]. Fluidized nanoparticles are expected to first form particle-particle clusters and then to form soft agglomerates from the clusters while the micron sized particles form particle-particle clusters [22]. The fluidized agglomerates were found to have a fractal dimension of 2.57 close to the predicted simulation value for diffusion limited agglomeration [22]. Wang et al. [23] showed a tiered arrangement of cluster sizes with large aggregates made of fine particles at the bottom (2.8 mm aggregates with 7 μm particles) and 0.3 mm aggregates from 17.8 μm average sized particles in the upper layer from particles 0.01 μm-18.1 μm in size. Several studies have shown that the application of force, through ultrasonic vibrations or other methods, will improve the fluidization behavior and generate a consistent agglomerate size [22,24–27]. It is hypothesized that the internal granule structures can also be controlled through changes in handling and the powder bed structure in traditional wet granulation applications. An imaging technique, such as X-ray tomography, capable of quantifying internal structures must be used to verify this hypothesis.

X-ray computed tomography (XRCT) is increasingly being used in a variety of applications as it provides detailed information about the internal structures of objects of interest [30]. This technique is capable of producing a 3-D recreation of the entire internal structure which allows for quantitative rather than qualitative structure analysis. Other techniques commonly used to describe granule structure, such as SEM, optical microscopy, and porosity measurements, do not provide information about the entire structure. XRCT has been used to calculate pore shape, size, connectivity and overall porosity for granules made from large particles. These values have been compared with those obtained from mercury porosimetry and were found to predict lower porosity and a larger pore size [31]. A different issue arises when attempting to determine porosity through tomography for ultra-fine powders. The smallest reported voxel resolution is on the order of 0.5-1 μm on a side, meaning that a single particle may be equal to or smaller than a single voxel. This resolution is insufficient to make a determination of granule micro-porosity and compare it to other methods [30]. XRCT is instead useful for examining meso-structures in ultrafine powder granules rather than porosity alone, which can be obtained from other methods. Recently published work by Dale et al. [32] describes a novel technique for measuring and describing phase distributions in granule microstructure which will be used for this study. The quantitative nature of this technique means that the impact of bed preparation, compaction, or other processing can be measured and compared to see which methods have the greatest impact.

This study tests the hypothesis that changes in powder bed preparation for ultra-fine powders will result in changes to the microstructure of wet granules. The effects of particle size on the complex behaviors will also be tested. It is hypothesized that the smallest particles will have the most complex behavior and increasing the particle size will simplify the behavior. Four different

size fractions of alumina powder are used. X-ray computed tomography is employed to examine and quantify changes in microstructure.

3. Materials and Methods

α-alumina particles with 4 different median particles sizes ((d_{50} = 0.5 µm, 5 µm, 25 µm, 108 µm Inframat Advanced Materials) were used to form granules for study. Particle size characterization was performed by wet dispersed laser diffraction (Malvern Mastersizer 2000). The 25 µm alumina dispersed easily in water with ultrasonics at 50%. A dispersant solution of IGEPAL CA-630 in water (1 g/1000 g water) was used to disperse the 0.5 and 5 µm powders. Particles were in the system for 5 minutes at 50% ultrasonic intensity before measurements were taken. The 108 µm particles broke up when dispersed (to around 1 µm) so a Tyler Ro-Tap Model E Sieve Shaker was used for sizing. The sieve shaker was run for 5 minutes using the Fine Analysis option. The powder flow properties have been evaluated using a Jenike & Johanson RST-XS Schulze Ring Shear Tester using 1,2, and 4 kPa pre-shear values with automatic shear-point selection.

Granules were prepared through single droplet nucleation in static, sieved beds. The powder was sifted through a single sieve into a petri dish (9 cm diameter) to prepare the powder beds. The two finest powders were sieved using 1.4 mm, 710 µm and 500 µm sieves. The 25 µm alumina easily passed through the 1.4 mm sieve and was sieved through the 710 µm and 500 µm sieves. The 108 µm alumina was very free flowing and passed easily through the 1.4 mm, 710 µm, and 500 µm sieves. Approximately 300 granules were created in each experiment using a 22 gauge needle from each powder/sieve combination. Water (2.71 ± 0.03 mm diameter droplets) was used as the binding liquid for submicron and 5 µm alumina powder beds. A solution of 0.05 g PVP K32 (manufacturer name) per gram of distilled water (2.76 ± 0.06 mm diameter droplets) was used for the 25 µm and 108 µm granules because the granules did not have sufficient dry strength for analysis with water as the binder. Granules were dried in a Mettler Toledo Halogen Moisture Analyzer at 100 °C. A Nikon SMZ1500 microscope was used for optical imaging of granules.

Ten granules from each experiment were randomly selected for XRCT imaging to examine and analyze the internal structure. A Scanco Medical microCT 40 (Purdue University) was used for the scans at its high resolution settings, resulting in a 6x6x6 µm voxel size. The material and sieve preparation will be referenced using the letter and number combinations in Table 1, such as Powder A1 or Powder B3.

Table 1: Reference Table of Different Powder and Sieve Combinations

Alumina Size (µm)	1.4 mm Sieved	710 µm Sieved	500 µm Sieved
0.5	A1	A2	A3
5	B1	B2	B3
25	C1	C2	C3
108	D1	D2	D3

The analysis of XRCT granule images was performed using ImageJ and MATLAB based on the analysis methodology developed by Dale et al. [32]. A binary threshold was applied in ImageJ using the automatic threshold selector to separate the granule from the background and non-granule pixels above the threshold limit are manually removed. This value is consistent between granules of a specific powder size fraction and production method. The edited images were processed in MATLAB to create a convex hull wrapping in the XY, YZ, and XZ planes and define the interior and exterior granule void space. Each distinct void was then labeled, with the center of mass, volume, volume equivalent sphere diameter, Feret's diameter, and surface area calculated. The Feret's diameter measurement code was obtained from the Mathworks File Exchange and was created by David Legland [33]. The measured and labeled voids were further processed to exclude small voids below a specific limit (micro-voids), either when viewing the stack as a 3-D reconstruction in ImageJ or during numerical evaluation of the voids. The 3-D reconstructions were created using the 3D Image Viewer plugin in ImageJ. An example of this process is shown in Figure 1.

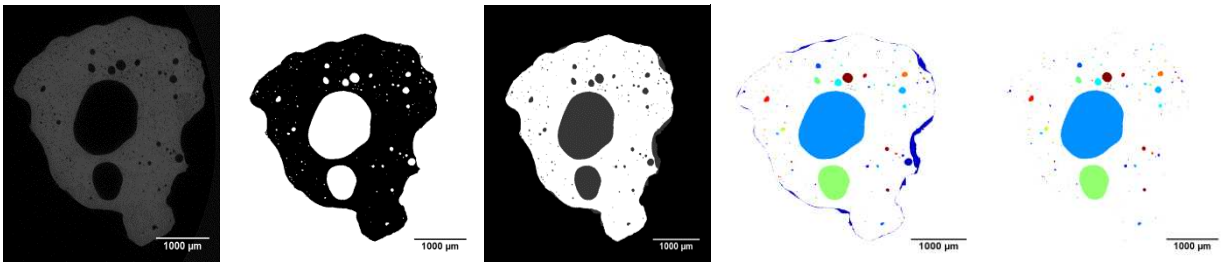

Figure 1: (A) Raw XRCT Slice, 0.5 µm Alumina (B) Segmented Particles (black) (C) Convex Hull Output (white=particle) (D) Color Coded Connectivity Map (E) External Void Removed

The processed stacks were evaluated using MATLAB. The minimum Feret's diameter of each 2D void was calculated in the XY plane and were removed if the diameter was less than the larger value of 5 times the voxel size (30 µm) or 3 times the primary particle D50. The minimum value was determined by calculating 7 different values at 30 degree intervals from 0 to 180 degrees and selecting the smallest value. This was repeated, in order, for the YZ and ZX planes. The total volume (in 3D) of the remaining voids, called macro-voids, was calculated by summing the voxel volume and converted to volume equivalent sphere diameters. The surface area of the 3D voids was also calculated using a simple counting of the number of exposed voxel faces for each labeled void. The sphericity of the labeled objects was then calculated to evaluate the shape of the macro-voids using the following equation:

$$\Psi_{void} = \frac{\pi^{\frac{1}{3}}(6V_{void})^{2/3}}{SA_{void}} \quad (1)$$

Where V_{void} is the volume of the labeled void in μm^3 as determined by counting voxels in the void and SA_{void} is the surface area in μm^2. The voids with $\Psi_{void} < 0.3$ were found to describe both cracks and external void fragments. Large external void fragments were manually removed by combining the labeled object center of mass with a visual inspection of labeled object stacks such as Figure 1D, 1E to confirm if the objects were internal or external voids. A single large external voids was removed from each Powder A and Powder B granule. All external voids above 150 µm equivalent sphere volume diameter were removed from Powder C and Powder D granules until 10 internal voids were found above that size limit. The fraction of granule volume (ε_{void}) contained in macro-voids was also calculated after the exclusions.

A radial distribution of the void space from the granule center of mass was created to look for repeating trends in the locations of the void volumes using 50 µm bins. An ellipsoid fitting function was used to look for preferential concentrations of voids at the top or bottom of granules using 50 µm bins. The distributions were normalized to the size of each granule to account for variations in granule size. The normalization was done by defining a maximum voxel distance (size) for each granule using the particle and void bins with more than 50 voxels. This maximum voxel distance was used to create normalized bins which represent 5% of the total axial or radial distance.

4. Results and Discussion

4.1. Powder Characteristics

The differences in size and shape between the powders can be observed using the SEM micrographs in Figure 2. The powder A in Fig 2A is a series of small particles which naturally cluster together and are viewed at resolutions of 1 µm or less. The particles of powder B in Fig 2B are sintered clusters of particles that resemble Powder A and are viewed at resolutison of 5 µm. The Powder C in Figure 2C is composed of jagged, irregularly shaped particles that are significantly different from Powders A and B. The Powder D particles in Figure 2D are actually spray-dried agglomerates that are composed of smaller primary particles.

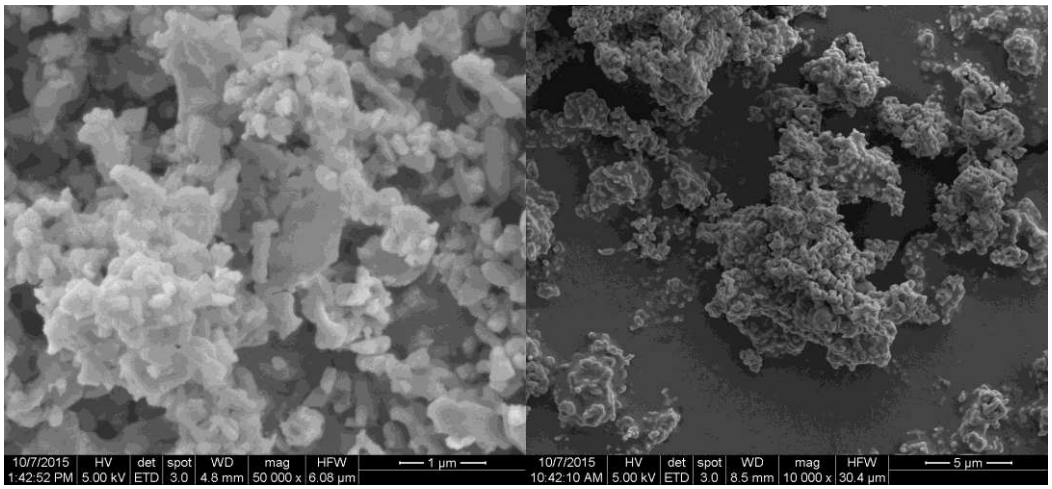

A B

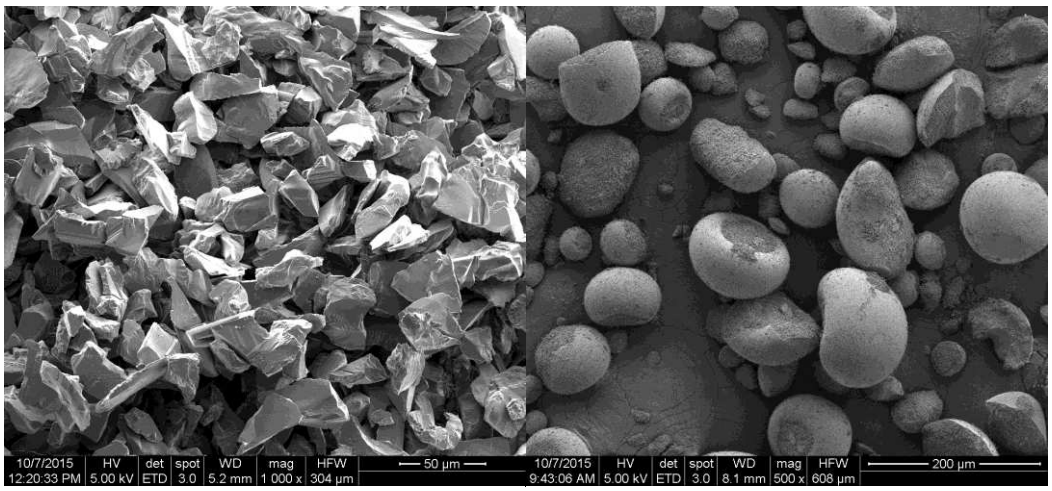

C D

Figure 2: SEM Micrographs (A) Powder A (B) Powder B (C) Powder C (D) Powder D

[Note: The scales are different in each figure as denoted by the scale bar in the bottom right of each figure.]

The light diffraction sizing data is shown in Figure 3 and generally confirms the estimates from observations made in Figure 2 regarding the size of primary particles. The sieve data for 108 µm particles in Figure 4 is also consistent with Figure 2D.

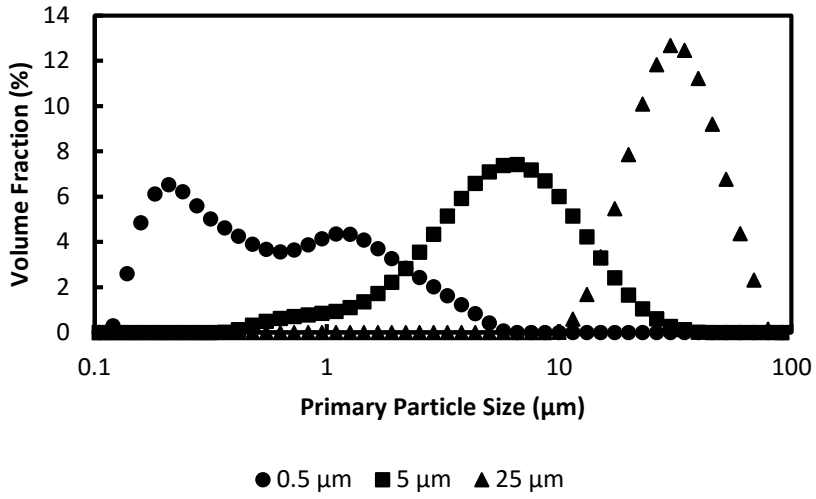

Figure 3: Particle size distribution of well dispersed alumina particles (Malvern Mastersizer 2000)

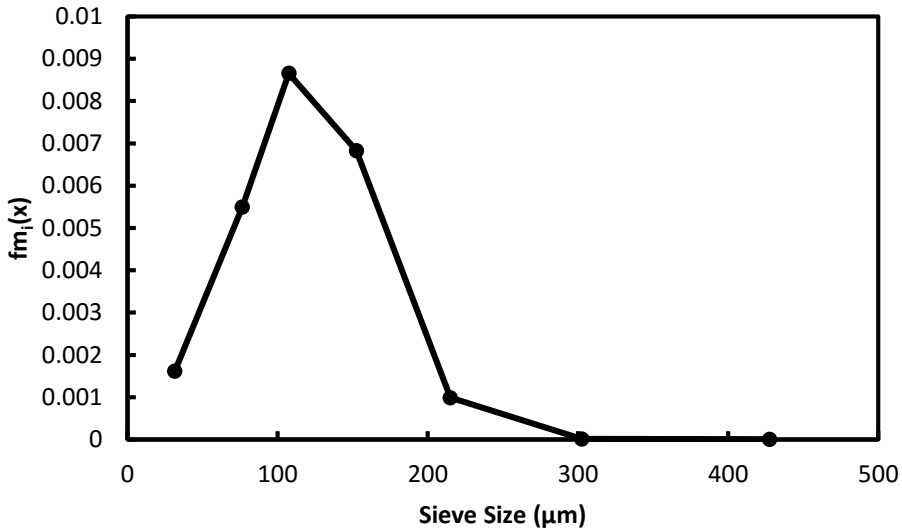

Figure 4: Particle size distribution of 108 micron aggregates (sieve size analysis)

The sizing data in Figure 3 shows that there are a large number of fine primary particles less than 1 µm and 0.5 µm in diameter for Powder A. The small particles were observed to aggregate over time when dispersed in water with ultrasonics, i.e. the size distribution shifted to the right with time. This is also consistent with Figure 2A where the primary particles naturally cluster. Typical d50 sizing for the 108 µm agglomerate primary particles are between 0.8-1.0 µm. The shear cell results in Figure 5 indicate that the 25 µm and 108 µm are exceptionally free flowing and the 0.5 µm and 5 µm particles are essentially non-flowing.

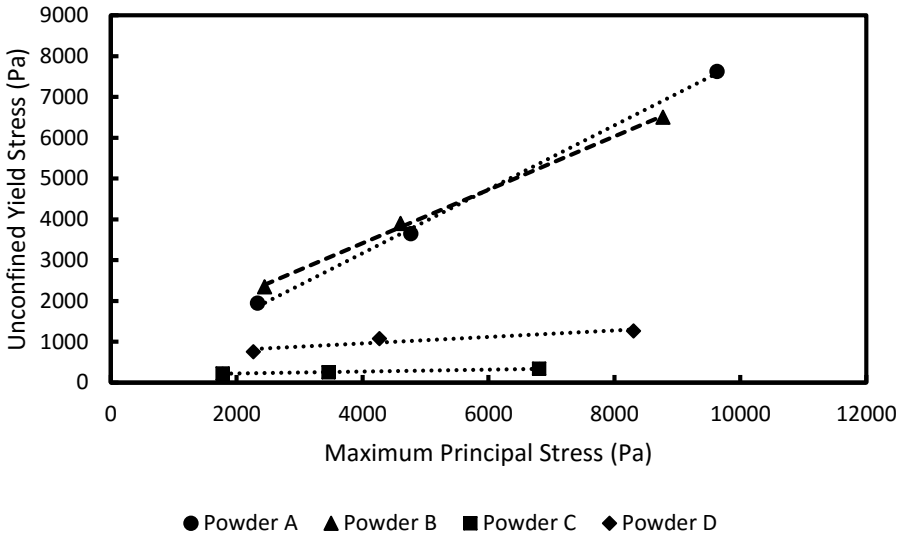

Figure 5: Ring Shear Tester results for alumina oxide powders

4.2. Analysis of Granule Structure

The various granule structures can be evaulated visually using an optical microscope, visual examination of XRCT image stacks and/or 3-D reconstructions of the void spaces. Representative images of the different visualization options are shown in Figures 6 to 8. The different size fractions of alumina each produce a distinct granule shape and internal structure when viewed through optical microscopy and XRCT image stacks.

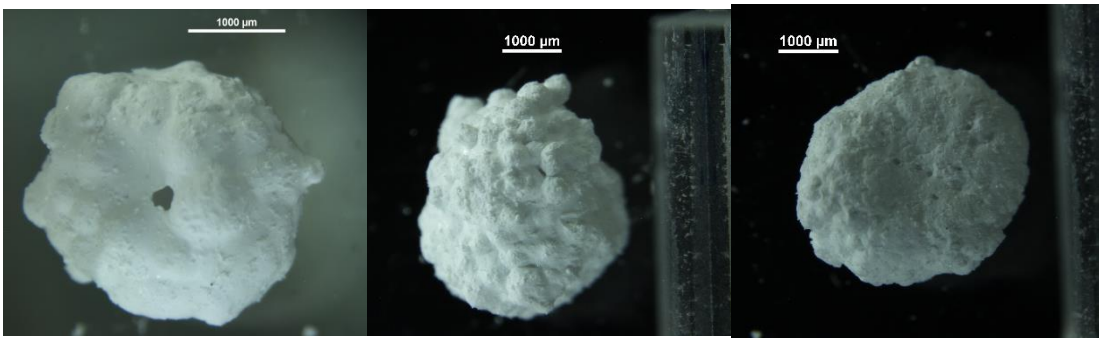

A **B** **C**

D **E** **F**

Figure 6: Microscope Images of alumina granules. (A) Powder A1 (B) Powder A2 (C) Powder A3 (D) Power B1 (E) Powder C1 (F) Powder D1

The optical microscopy images in Figure 6 shows the different alumina particle sizes produce different granule shapes. Powder A granules (Fig 6A-6C) are made up of smaller spherical aggregates that appear to vary in size with sieve preparation. Powder A1 in Fig 6A has the largest aggregates and Powder A3 in Fig 6C has the smallest aggregates. The granules are round with a concave indentation at the top, relative to the orientation when formed. Powder B granules (Fig 6D) are rounded and smoothed with no visual differentiations from orientation or sieve preparation. Powder A and Powder B granule shapes are consistent with the Tunneling mechanism as expected from primary particle size [7]. Powder C granules (Fig 6E) resemble a mushroom with a circular core at the top of the granule and a rounded cap at the bottom. Powder D granules (Fig 6F) are a thin relatively thin concave disk less than 2 mm thick. Powder C and Powder D granule shapes are consistent with the Spreading/Crater mechanism of drop granule formation [7].

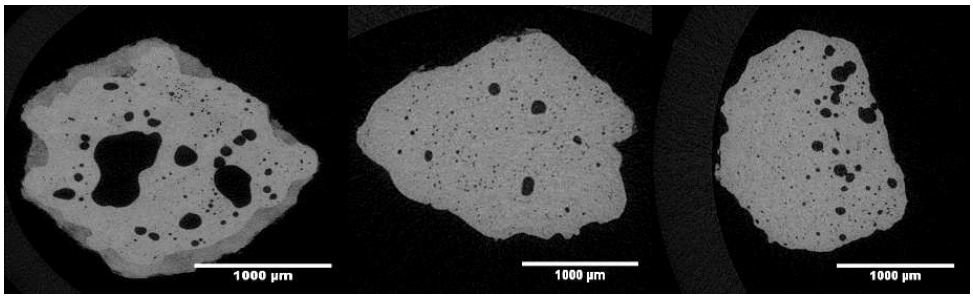

A **B** **C**

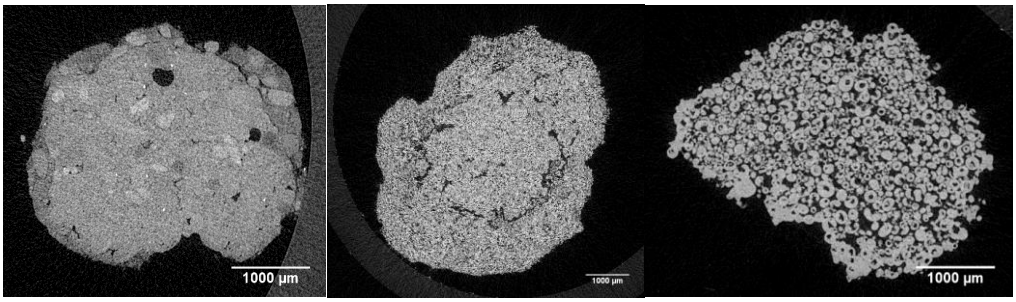

D **E** **F**

Figure 7: Representative XRCT Slices. (A) Powder A1 (B) Powder A2 (C) Powder A3 (D) Power B1 (E) Powder C1 (F) Powder D1 [Note: Granule contrast has been increased to improve object visibility in print]

The XRCT slices in Figure 7 show that there is also a significant effect from changing the primary particle size on the granule internal structure. Powder A granules in Fig 7A-7C show a number of large, discrete void spaces surrounded by a dense particle matrix. Powder A primary particles are smaller than the 6 µm voxel resolution so the "solid" areas of the image are actually made up of a mixture of primary particles and pores. The voids in Fig 7A are noticeably larger than those in Fig 7B or 7C. The largest voids in Fig 7C appear to cluster to one side of the granule, which is the top of the granule when the formation orientation is considered. The Powder B granule microstructures in Fig 7D have a few large, discrete void spaces, but is mostly the particle matrix. Powder C granules in Fig 7E have some large cracks that are centered on the circular core observed in Fig 6E and a diffuse pore network elsewhere. Fig 7F shows that the Powder D particles are actually hollow spray-dried aggregates which is consistent with SEM images of the powder (Fig. 2D). The internal structure is that of a pore network which is expected with large particles and a handful of isolated voids within the spray-dried agglomerates.

The use of 3D representations in Figure 8 allows for better visualization of the entire structure of a granule than looking at the 2D slices individually. Here, the colored objects are the macro-voids within the granule. Objects of identical color are connected in 3D. Powder A granules in Fig 8 A-C can be fully visualized because the external void space is easily removed. Figure 8A shows the existence of large macro-voids that travel throughout the granules formed from Powder A1. The large orange void at the center and the light blue void in the lower right of Figure 8A are prime examples of this behavior with large necks formed between sections. The macro-voids are clearly smaller in Fig 8B & 8C but are still large distinct objects within the granules. This shows that preparing Powder A using different sieves creates differences in the maximum size of macro-voids within the granules. Figure 8D and 8E show the results of external void fragmentation during processing. The large voids at the edges of Figure 8E have all been removed manually from the size/volume analysis as discussed in Section 3. Figure 8F shows that the external void fragmentation for Powder D granules the remaining macro-voids are thin slices at the outer edges and are not internal to the granule.

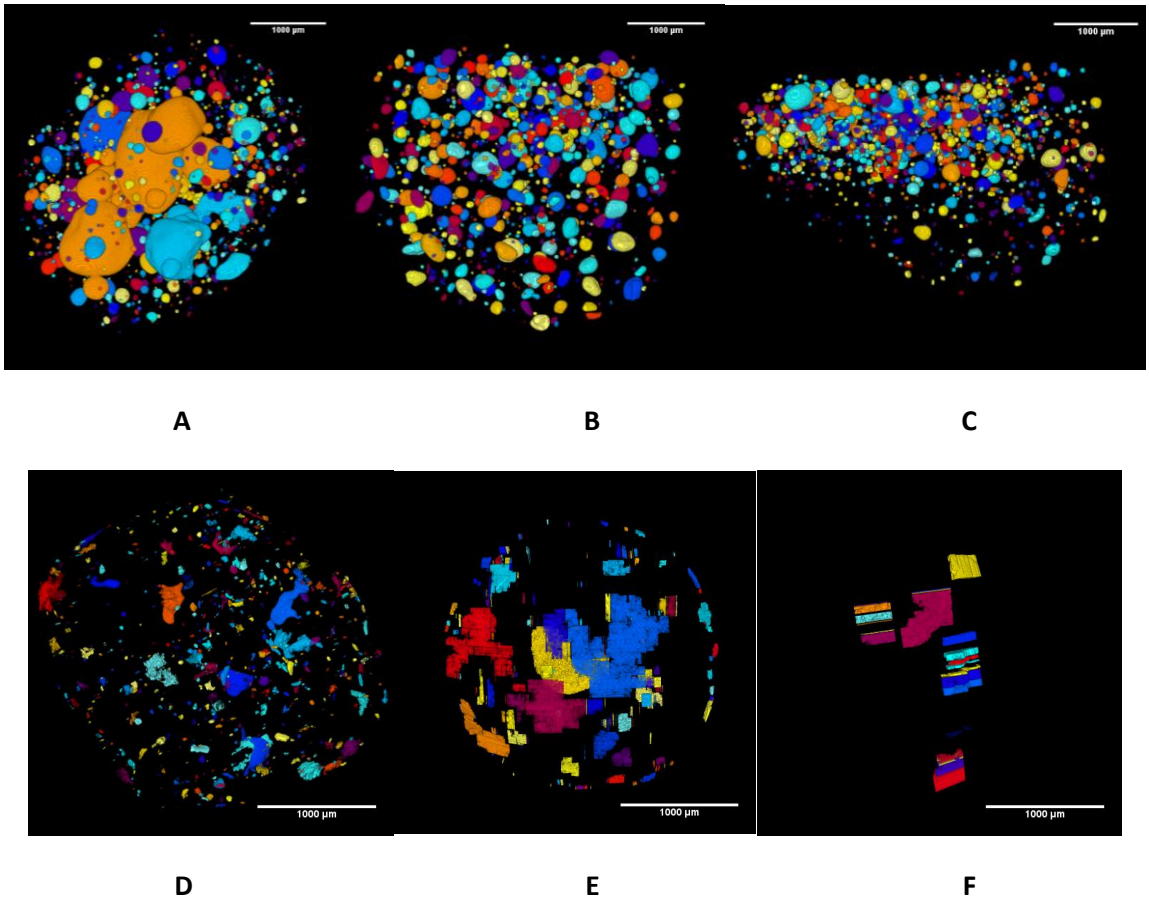

Figure 8: 3D macro-void reconstruction (A) Powder A1 (B) Powder A2 (C) Powder A3 (D) Power B1 (E) Powder C3 (F) Powder D1 (Created using ImageJ)

4.3. Effects of Primary Particle Size

Changing the primary particle size clearly shifts the nuclei formation mechanism. Powder A (Fig 5A, B, C) and Powder B (Fig 5D) granules are formed through the Tunneling mechanism and are mostly round. The Powder C (Fig 5E) and Powder D (Fig 5F) granules are clearly formed through the Crater/Spreading mechanism. Powder C granules have the expected mushroom stalk/cape shape. Powder D granules are best described as thin, concave wafers formed only at the surface of the powder bed. The large particles can clearly be seen for Powder D granules and large agglomerates can also be seen in some of Powder A granules.

There are also clear qualitative effects on granule microstructure from the changes in particle size. Powder A granules (Fig 6-A,B,C) show a solid matrix filled with many large, discrete macro-voids. The dense solid phase, which appears continuous with some variations in density, is actually a mixture of primary particles and pores. The primary particles are an order of magnitude smaller than the voxel resolution (6x6x6 µm) so small spaces between particles are not visible. Powder B (Fig 6-D) granules have a solid matrix with some large, discrete

macro-voids but fewer and smaller visually than those in the 0.5 µm granules. Powder C (Fig 6-E) produces a discrete network of particles and voids with the spaces between particles visible. There are some large macro-voids that are best described as cracks in the Powder C and the rest of the voids are micro-voids. Powder D (Fig 6-F) shows that it has a pore network made up of small spray-dried granules.

There is a strong effect from changing primary particle size on the percentage of the total granule volume contained in macro-voids or ε_{void} (Figure 9). Powder A1 granules have average ε_{void} values of 7% and as high as 9% while the Powder D granules have average ε_{void} values of at or near 0. Decreasing the primary particle size causes the ε_{void} value to increase both for ultra-fine powders and non-ultra-fine powders. The change in the granule nucleation mechanism from Powder B to Powder C results in an increase in ε_{void} due to crack formation around the "stem" of the mushroom shaped granule.

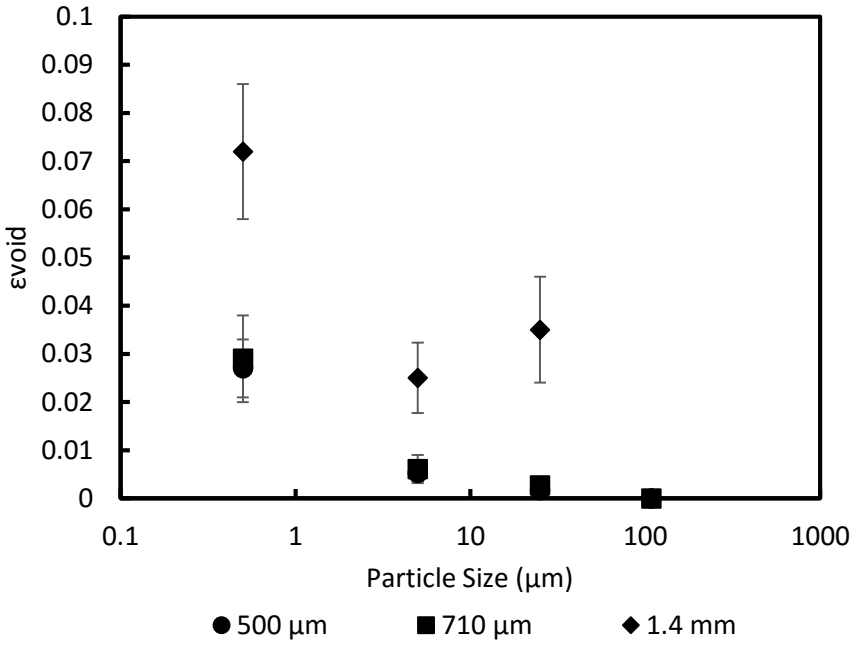

Figure 9: Fraction of total granule volume contained in macro-voids

A similar effect exists for the maximum macro-void size in each granule shown in Figure 10. A decrease in primary particle size strongly correlates with an increase in the maximum volume/size of macro-voids. The largest macro-voids in Powder B1 are two thirds the size of those in Powder A1 which have an equivalent sphere volume diameter of 883 µm. A typical Powder A or Powder B granule is approximately 3 mm in diameter. A typical powder C granule is approximately 4 mm across. There are no macro-voids in Powder D granules.

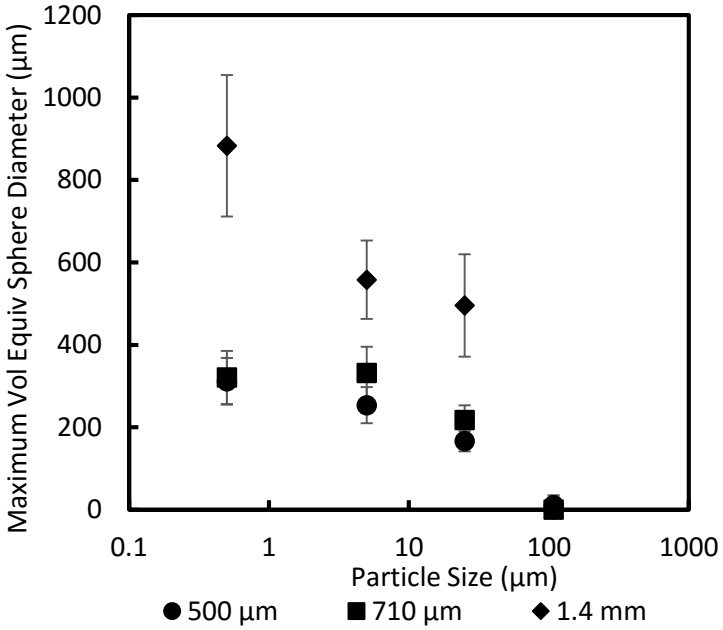

Figure 10: Average size of largest individual macro-voids

4.4. Effects of Bed Preparation

There is a strong effect of bed preparation on the microstructure of Powder A granules. The effects on ε_{void} and macro-void size can be seen in Figures 6-10 in both the visual observations and the quantitative measurements. Powder A1 granules have macro-voids which are visibly larger than the macro-voids in Powders A2 & A3 and this is confirmed by the measurements reported in Figure 10. There is a similar effect seen in the ε_{void} values in Figure 9. The change in sieve size from Powder A2 to Powder A3 does not cause a similar change as seen in either ε_{void} and macro-void volume. The maximum macro-void sizes in Powder A2 & A3 are 310 and 320 µm respectively, although the shape of these voids is very different.

There is a weaker effect of bed preparation on the microstructure of Powder B granules than for Powder A. The data in Figure 9 and Figure 10 show that Powder B1 granules have more and larger macro-voids than Powders B2 & B3. There are no discernible effects of bed preparation on the volume or size of macro-voids in Powder C and Powder D granules. There are no changes to the nuclei formation mechanism from changes in bed preparation.

The observed effect of bed preparation on the distribution of macro-voids in Powder A granules must be evaluated in a different fashion. The 3D reconstruction of the Powder A3 Granule in Figure 8C shows that the macro-voids appear to cluster towards the top of the granule based

upon the granule orientation during formation. The top of the granule is identified by the concave surface seen in Figure 5C. The axial distribution is the appropriate method for evaluating this. Figure 11 shows the axial distribution results for macro-void volume in Powders A1-A3 and it does show the clustering near the top of the granule for Powder A3. However, there is not a clear transition of macro-void position from Powder A1 to Powder A3. It is unclear if this is random variation as a result of small sample size or evidence of a second-order effect related to the bed preparation. However, the available information is sufficient to show that the analysis method is capable of picking up such a change in distribution if it should occur.

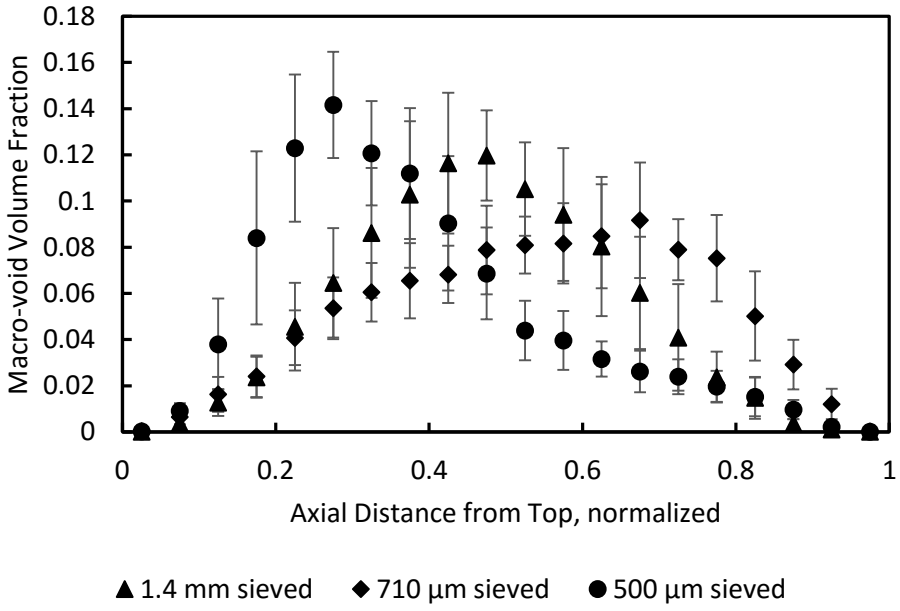

Figure 11: Axial distribution for 0.5 µm alumina granules. Describes distribution of macro-void volume as a fraction of total macro-void volume.

4.5. Discussion

The presence of strong cohesive forces creates the potential for complex structures in the powder bed. Large particles with little or no cohesive strength will form a relatively homogenous bed with consistent macro-,meso-,and micro-structures throughout the bed. The presence of strong cohesive forces creates the potential for complex structures of varying size within the powder bed. This leads to volumes of differing density and the creation of large scale, relatively stable structures. These different structures will interact with the liquid droplet at different rates and can break up if the larger structures have cracks or other flaws in them.

The quantifiable differences in structure come, in part, from the dominant attractive forces present in the 0.5 µm particles. The images of the sieved 0.5 µm particles in Figure 15 show that the powder forms small agglomerates of varying sizes. The different sizes of small aggregates

likely contributes to differences in the packing of the bed structure. The maximum size is greatest for the 1.4 mm sieving which also has a wider size distribution of the aggregates. The larger size distribution of agglomerates should result in a more varied bed structure. The larger structures are also more likely to break up because of flaws in the agglomerate. One possible explanation for the existence of macro-voids in the drop formed granules is that they already exist in the bed before liquid is added. Another is that the voids are primarily formed during drying in a fashion similar to that described by Pagnoux et. al. [21]. Certain high density, closely packed areas would have low particle mobility and lower density areas would have high particle mobility which leads to the existence of many macro-voids rather than a completely hollow structure. The former theory, that the structures existed to begin with, is more likely because the "drying" model would mean granule structure is independent of bed preparation. The rate at which the granules are dried may also have some second-order effects on the precise macro-void size.

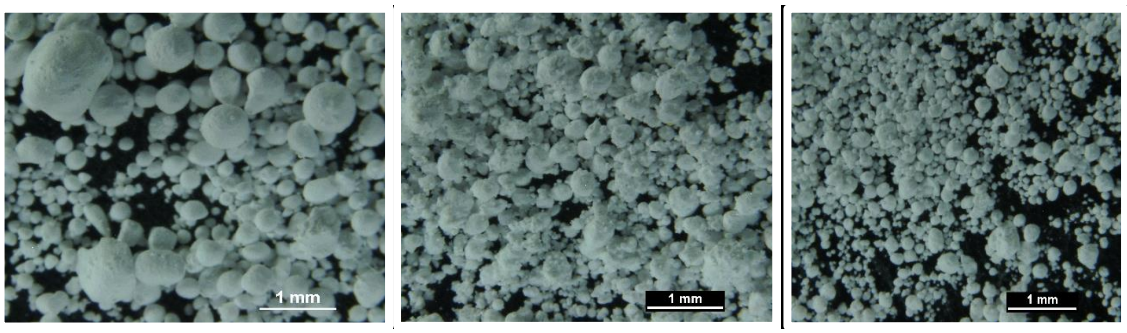

Figure 12: 0.5 µm primary particles that have been passed through different sieve sizes. (A) A1 (B) A2 (C) A3

The more cohesive the material is, the greater the potential for complex structures to exist in the bed. The more complex structures that exist in the powder bed, the larger the number and/or size of macro-voids with a granule This would explain why Powder A granules have more and larger macro-voids than Powder B granules after sieving. The switch to larger, non-cohesive reduces the opportunity for complex structures.

The study and description of granule microstructure in literature is sparse, especially for small particles. However, there are a variety of different microstructures that exist dependent up on the particle size. These different structures need to be characterized in a quantitative manner to describe the effects of process changes. There is the potential for very large macro-voids to exist within granules separate from the hollow structures that can be found in certain processes. The methods described in this paper show how to quantify changes in these macro-voids based on size, shape, and location within the granule. It also allows for identification and differentiation between external void space, pore networks, cracks, and macro-voids. The powder handling history has also been shown to have an impact on the structure of the smallest materials. The

handling history has little observed effect for the larger powders. These observations explain the anecdotal evidence from industrial application that granulation of ultra-fine powders can be highly variable and highly sensitive to powder history.

The impacts of these different microstructures and handling histories on the further processing of granules is unstudied. However, granules that are hollow or have large macro-voids can be considered to have flaws of various sizes. These flaws introduce potential weaknesses into the granule structure and can affect granule properties, such as strength, and make the granules more likely to break than their homogenous counterparts. This is the theory promoted by Kendall which argues that fracture strength scales with the negative square root of of the flaw size [34]. Thus, the strength of granules formed from ultra-fine powders can be much lower than expected unless care is taken to remove macro-voids.

It is also possible that additional, vigorous processing of the powders will override the previous history. The exact method of handling is likely to be important as a fluidized bed provides very different stresses on the granules than a screw feeder or vibrating tray and all are different from a static, sieved bed. A fluidized bed arrangement is the one most likely to show effects similar to those from bed preparation shown in this paper [22-29]. Powder mixtures including particles that differ in size by orders of magnitude are not expected to show effects from handling history because the larger particles are expected to be dominant.

6. Conclusions

This work successfully demonstrates a method for analyzing 3D granular meso-structures using XRCT. This method has been shown to be capable of distinguishing between pore networks, cracks and large, discrete macro-voids that exist in granules formed from various sized primary particles that are chemically similar. It makes use of macro-void sphericity and volume as primary descriptors to distinguish between different types of structures. This method can be used to distinguish between differences brought on by changes in the production process. It can be used, for example, to supplement porosity measurements by giving a precise explanation of how structure has changed in the granule.

Ultra-fine powders have complex behaviors and the effect becomes stronger as the particle size is decreased. Chemically similar materials can be made to form radically different granule structures simply by changing the size of the primary particles. Sub-micron primary particles are capable of forming granules with large, discrete macro-voids of various shapes and sizes. Therefore, the size distribution of feed materials must be tightly controlled to ensure consistent and reproducible behaviors in granulated materials.

The prior handling of ultra-fine powders has also been shown to have an impact on material behavior and the granule microstructure. Due to natural agglomeration of fine particles, this effect is strongest for the smallest particles. Other systems which can induce this behavior, such as fluidized beds, have the potential for similar issues. It also shows the need for greater care with the handling and preparation histories of ultra-fine powders because it can profoundly effect final granule properties.

7. Acknowledgements

Thank you to the Purdue Nutrition Science Department for the use of their CT equipment.

8. References

[1] S.M. Iveson, J.D. Litster, K. Hapgood, B.J. Ennis, Nucleation, growth and breakage phenomena in agitated wet granulation processes: a review, Powder Technol. 117 (2001) 3–39. doi:10.1016/S0032-5910(01)00313-8.

[2] J. Visser, Van der Waals and Other Cohesive Forces Affecting Powder Fluidization, Powder Technol. 58 (1989) 1–10.

[3] K.P. Hapgood, J.D. Litster, S.R. Biggs, T. Howes, Drop penetration into porous powder beds., J. Colloid Interface Sci. 253 (2002) 353–66. doi:10.1006/jcis.2002.8527.

[4] N. Eshtiaghi, B. Arhatari, K.P. Hapgood, Producing hollow granules from hydrophobic powders in high-shear mixer granulators, Adv. Powder Technol. 20 (2009) 558–566. doi:10.1016/j.apt.2009.08.006.

[5] N. Eshtiaghi, J.J.S. Liu, K.P. Hapgood, Formation of hollow granules from liquid marbles: Small scale experiments, Powder Technol. 197 (2010) 184–195. doi:10.1016/j.powtec.2009.09.013.

[6] N. Eshtiaghi, K.P. Hapgood, A quantitative framework for the formation of liquid marbles and hollow granules from hydrophobic powders, Powder Technol. 223 (2012) 65–76. doi:10.1016/j.powtec.2011.05.007.

[7] H.N. Emady, D. Kayrak-Talay, W.C. Schwerin, J.D. Litster, Granule formation mechanisms and morphology from single drop impact on powder beds, Powder Technol. 212 (2011) 69–79. doi:10.1016/j.powtec.2011.04.030.

[8] J. Fu, M.J. Adams, G.K. Reynolds, a. D. Salman, M.J. Hounslow, Impact deformation and rebound of wet granules, Powder Technol. 140 (2004) 248–257. doi:10.1016/j.powtec.2004.01.012.

[9] K.P. Hapgood, B. Khanmohammadi, Granulation of hydrophobic powders, Powder Technol. 189 (2009) 253–262. doi:10.1016/j.powtec.2008.04.033.

[10] H. Charles-Williams, R. Wengeler, K. Flore, H. Feise, M.J. Hounslow, A.D. Salman,

Granulation behaviour of increasingly hydrophobic mixtures, Powder Technol. (2012). doi:10.1016/j.powtec.2012.06.009.

[11] S.L. Rough, D.I. Wilson, D.W. York, Effect of solids formulation on the manufacture of high shear mixer agglomerates, Adv. Powder Technol. 16 (2005) 145–169. doi:10.1163/1568552053621704.

[12] K. van den Dries, H. Vromans, Quantitative proof of liquid penetration-involved granule formation in a high shear mixer, Powder Technol. 189 (2009) 165–171. doi:10.1016/j.powtec.2008.04.007.

[13] M. Shafiee Afarani, A. Samimi, E. Bahadori Yekta, Synthesis of alumina granules by high shear mixer granulator: Processing and sintering, Powder Technol. 237 (2013) 32–40. doi:10.1016/j.powtec.2013.01.007.

[14] S.. Rough, D.. Wilson, a Bayly, D. York, Tapping characterisation of high shear mixer agglomerates made with ultra-high viscosity binders, Powder Technol. 132 (2003) 249–266. doi:10.1016/S0032-5910(03)00075-5.

[15] K. Saleh, L. Vialatte, P. Guigon, Wet granulation in a batch high shear mixer, Chem. Eng. Sci. 60 (2005) 3763–3775. doi:10.1016/j.ces.2005.02.006.

[16] S.L. Rough, D.I. Wilson, a. E. Bayly, D.W. York, Mechanisms in high-viscosity immersion–granulation, Chem. Eng. Sci. 60 (2005) 3777–3793. doi:10.1016/j.ces.2005.02.013.

[17] R.P.J. Sochon, S.K. Dorvlo, a. I. Rudd, I. Hayati, M.J. Hounslow, a. D. Salman, Granulation of Zinc Oxide, Chem. Eng. Res. Des. 83 (2005) 1325–1330. doi:10.1205/cherd.05099.

[18] a Johansen, T. Schaefer, Effects of physical properties of powder particles on binder liquid requirement and agglomerate growth mechanisms in a high shear mixer., Eur. J. Pharm. Sci. 14 (2001) 135–47. http://www.ncbi.nlm.nih.gov/pubmed/11500259.

[19] K. Žižek, M. Hraste, Z. Gomzi, High shear granulation of dolomite – I: Effect of shear regime on process kinetics, Chem. Eng. Res. Des. (2012) 1–17. doi:10.1016/j.cherd.2012.06.014.

[20] S. Eckhard, M. Nebelung, Investigations of the correlation between granule structure and deformation behavior, Powder Technol. 206 (2011) 79–87. doi:10.1016/j.powtec.2010.06.002.

[21] C. Pagnoux, N. Tessier-Doyen, A. Pringuet, M. Cerbelaud, P. Garcia-Perez, Influence of the suspension flocculated state on the microstructure of alumina spheres elaborated by colloidal granulation, J. Eur. Ceram. Soc. 29 (2009) 1379–1385. doi:10.1016/j.jeurceramsoc.2008.09.007.

[22] J.R. van Ommen, J.M. Valverde, R. Pfeffer, Fluidization of nanopowders: a review., J. Nanopart. Res. 14 (2012) 737. doi:10.1007/s11051-012-0737-4.

[23] Z. Wang, M. Kwauk, H. Li, Fluidization of fine particles, Chem. Eng. Sci. 53 (1998) 377–395.

[24] C. Xu, J. Zhu, Parametric study of fine particle fluidization under mechanical vibration, Powder Technol. 161 (2006) 135–144. doi:10.1016/j.powtec.2005.10.002.

[25] C. Xu, J. Zhu, Experimental and theoretical study on the agglomeration arising from fluidization of cohesive particles—effects of mechanical vibration, Chem. Eng. Sci. 60 (2005) 6529–6541. doi:10.1016/j.ces.2005.05.062.

[26] L. Zhou, H. Wang, T. Zhou, K. Li, H. Kage, Y. Mawatari, Model of estimating nano-particle agglomerate sizes in a vibro-fluidized bed, Adv. Powder Technol. 24 (2013) 311–316. doi:10.1016/j.apt.2012.08.002.

[27] Y. Mawatari, M. Tsunekawa, Y. Tatemoto, K. Noda, Favorable vibrated fluidization conditions for cohesive fine particles, Powder Technol. 154 (2005) 54–60. doi:10.1016/j.powtec.2005.04.026.

[28] Y.-D. Liu, S. Kimura, Fluidized-bed nitridation of fine silicon powder, Powder Technol. 106 (1999) 160–167. doi:10.1016/S0032-5910(99)00072-8.

[29] T. Nakazato, J.-I. Kawashima, T. Masagaki, K. Kato, Penetration of fine cohesive powders through a powder–particle fluidized bed, Adv. Powder Technol. 17 (2006) 433–451. doi:10.1163/156855206777866128.

[30] S.R. Stock, Recent advances in X-ray microtomography applied to materials, Int. Mater. Rev. 53 (2008) 129–181. doi:10.1179/174328008X277803.

[31] L. Farber, G. Tardos, J.N. Michaels, Use of X-ray tomography to study the porosity and morphology of granules, Powder Technol. 132 (2003) 57–63. doi:10.1016/S0032-5910(03)00043-3.

[32] S. Dale, C. Wassgren, J. Litster, Measuring granule phase volume distributions using X-ray microtomography, Powder Technol. 264 (2014) 550–560. doi:10.1016/j.powtec.2014.06.009.

[33] D. Legland, Feret diameter and oriented box v1.1, (2014). http://www.mathworks.com/matlabcentral/fileexchange/30402-feret-diameter-and-oriented-box.